Distinct kinetic mechanisms of H3K4 methylation catalyzed by MLL3 and MLL4 core complexes

Yongxin Zheng[1], Yinping Huang[1,‡], Jun Mencius[1,‡], Yanjing Li[2], Lijie Zhao[2,3], Wanting Luo[2,3,4], Yong Chen[2,3,4,*], and Shu Quan[1,*]

From the [1]State Key Laboratory of Bioreactor Engineering, Shanghai Collaborative Innovation Center for Biomanufacturing (SCICB), East China University of Science and Technology, Shanghai, China; [2]State Key Laboratory of Molecular Biology, Shanghai Institute of Biochemistry and Cell Biology, Center for Excellence in Molecular Cell Science, Chinese Academy of Sciences, Shanghai, China; [3]University of Chinese Academy of Sciences, Beijing, China; [4]School of Life Science and Technology, ShanghaiTech University, Shanghai, China

Edited by John Denu

The methyltransferases MLL3 and MLL4 primarily catalyze the monomethylation of histone H3 lysine 4 (H3K4) on enhancers to regulate cell-type-specific gene expression and cell fate transition. MLL3 and MLL4 share almost identical binding partners and biochemical activities, but perform specific and nonredundant functions. The features and functions that distinguish MLL3 and MLL4 remain elusive. Here, we characterize the kinetic mechanisms of MLL3 and MLL4 ternary complexes containing the catalytic SET domain from MLL3 or MLL4 (MLL3$_{SET}$ or MLL4$_{SET}$), the SPRY domain of ASH2L (ASH2L$_{SPRY}$), and a short fragment of RBBP5 (RBBP5$_{AS-ABM}$) to search for possible explanations. Steady-state kinetic analyses and inhibition studies reveal that the MLL3 complex catalyzes methylation in a random sequential bi–bi mechanism. In contrast, the MLL4 complex adopts an ordered sequential bi–bi mechanism, in which the cofactor S-adenosylmethionine (AdoMet) binds to the enzyme prior to the H3 peptide, and the methylated H3 peptide dissociates from the enzyme before S-adenosylhomocysteine (AdoHcy) detaches after methylation. Substrate-binding assays using fluorescence polarization (FP) confirm that AdoMet binding is a prerequisite for H3 binding for the MLL4 complex but not for the MLL3 complex. Molecular dynamic simulations reveal that the binding of AdoMet exclusively induces conformational constraints on the AdoMet-binding groove and the H3 substrate-binding pocket of MLL4, therefore stabilizing a specific active conformation to ease entry of the substrate H3. The distinct kinetic mechanisms and conformational plasticities provide important insights into the differential functions of MLL3 and MLL4 and may also guide the development of selective inhibitors targeting MLL3 or MLL4.

Methylation of histone H3 lysine 4 (H3K4), generally regarded as a marker for transcriptional activation, has implications in hematopoiesis (1, 2), embryonic development (3, 4), and memory retrieval (5). H3K4 methylation patterns are mainly established by the histone-lysine N-methyltransferase 2 (KMT2) family proteins, which are conserved from yeast to human (6). Mammalian KMT2 family, also known as mixed-lineage leukemia (MLL) family, consists of six members (MLL1-MLL4, SET1A, and SET1B), each of which exhibits specific functions (7, 8). SET1A (KMT2F) and SET1B (KMT2G) mediate widespread H3K4 trimethylation (H3K4me3) at promoter regions of housekeeping genes (8). MLL1 (KMT2A) and MLL2 (KMT2B) are mainly responsible for dimethylation and trimethylation (H3K4me2/3) at promoter regions (9, 10). MLL3 (KMT2C) and MLL4 (KMT2D) primarily catalyze the H3K4 monomethylation at enhancer regions to activate the enhancers (11, 12).

MLL3 and MLL4, two paralogs in the KMT2 subfamily, share similar domain organization and identical interacting proteins (Fig. 1). MLL3 and MLL4 both have a series of PHDs (Plant Homeotic Domains) (eight in MLL3 and seven in MLL4), an HMG (High Mobility Group) domain, a separated FY-rich-domain-containing FYRN (F/Y-rich N-terminus) and FYRC (F/Y-rich C-terminus), and a C-terminal SET [SU(VAR) 3–9, E(Z), and TRX] domain. MLL3 and MLL4 form multi-subunit complexes in the cells to exert their methylation activities. The optimal methyltransferase activities of MLL3/4 require the association of four regulatory proteins, WDR5 (WD Repeat-containing protein 5), ASH2L (Absent-Small-Homeotic-2-Like protein), RBBP5 (RetinoBlastoma Binding Protein 5), and DPY30 (DumPY-30), which are also the shared binding partners for other KMT2-family methyltransferases (13, 14). In addition, MLL3 and MLL4 associate with the same set of specific accessory components, which are unique for the MLL3/4-branch KMT2 subfamily, including PTIP (Paired box (Pax) transactivation-domain interacting protein), PA1 (PTIP-associated 1), NCOA6 (Nuclear receptor COActivator 6), and KDM6A (Lysine Demethylase 6A, also known as UTX) (15). Apart from the identical complex composition, MLL3 and MLL4 complexes also possess many similar biochemical activities. For example, they both catalyze the monomethylation of H3K4 through C-terminal catalytic SET domains activated by associating with ASH2L-RBBP5 heterodimer directly (11, 14). Moreover, both the PHD6 domain of MLL4 and the

---
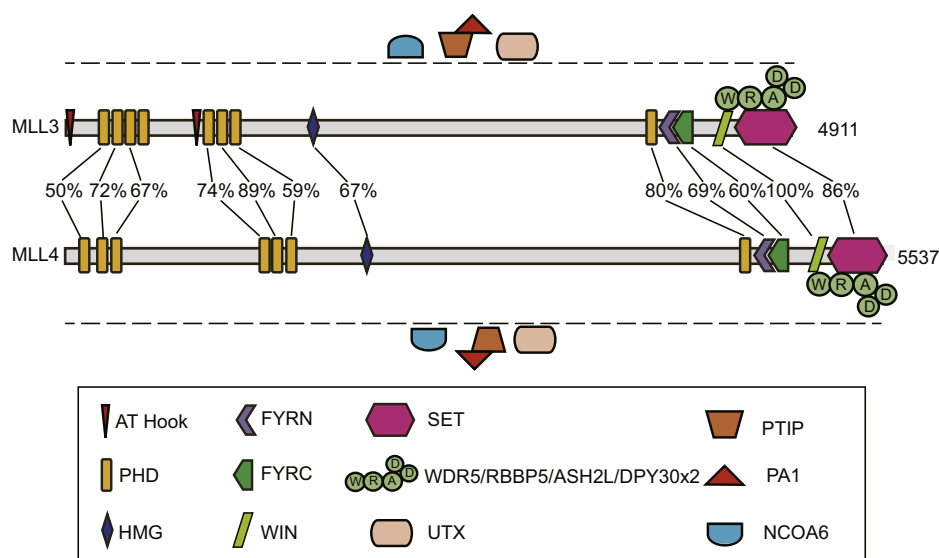
Figure 1. Schematic representation of the domain organization and components association for MLL3 and MLL4. MLL3 and MLL4 share the similar domain organization and identical interacting proteins. The sequence identities between each domain of MLL3 and MLL4 are obtained by amino acid sequence alignment based on EMBOSS Needle (59). FYRC, F/Y-rich C- terminus; FYRN, F/Y-rich N- terminus; HMG, high-mobility group; PHD, plant homeotic domain; SET, SU(VAR)3–9, E(Z) and TRX; WIN, WDR5 interaction.

corresponding PHD7 domain of MLL3 can bind to the H4 tail and specifically recognize H4K16Ac modification (16–18).

Despite the indistinguishable biochemical properties of MLL3 and MLL4, their functions are not identical. Knockouts of *Mll3* and *Mll4* in mice generate distinct phenotypes. *Mll3*-knockout mice showed no significant morphological abnormalities during embryonic development but died around birth (4). Mechanistically, loss of *Mll3* caused defects in lung maturation and respiratory failure at birth (19). In contrast, *Mll4*-knockout mice died at 9.5 days of embryonic life (4), because *Mll4* was required for migration of the anterior visceral endoderm (AVE) to initiate gastrulation (19, 20). Consistent with their nonredundant roles in cell fate transition, mutations of MLL3 and MLL4 are identified in different types of diseases and cancers. For example, a number of heterozygous MLL4 variants cause Kabuki syndrome, a rare congenital disorder disease, but MLL3 mutation has never been reported in Kabuki syndrome (21). These results demonstrate that MLL3 and MLL4 have their unique functions in cells.

The apparent discrepancy between almost identical biochemical properties and distinct physiological functions intrigues us to investigate whether there is any potential biochemical difference between MLL3 and MLL4. We focus on the possible catalytic difference between MLL3 and MLL4, because their enzyme activities are critical for enhancer activation in ESC differentiation and adipogenesis (22–24). The catalytic domains of MLL3 and MLL4 have been structurally characterized (14, 25), but the research on the kinetic mechanism of MLL3 or MLL4-mediated catalytic process is still limited. Here, we use a continuous enzyme-coupled assay to elucidate the kinetic mechanisms of the minimized ternary complexes composed of the catalytic domains of MLL3 or MLL4 (MLL3$_{SET}$ or MLL4$_{SET}$), ASH2L, and RBBP5.

Steady-state kinetic analyses and inhibition studies reveal that the MLL3 complex catalyzes monomethylation of the histone H3 peptide with a random sequential bi–bi mechanism. On the contrary, the MLL4 complex utilizes an ordered sequential bi–bi mechanism. The difference of the conformational dynamics between MLL3 and MLL4 may result in the distinct kinetic mechanism. The unforeseen catalytic difference revealed in our work may provide critical insight into the distinct functions of MLL3 and MLL4 and give hints for inhibitor design targeting MLL3 or MLL4.

Results

Steady-state kinetic properties of M3RA and M4RA on H3 peptides

The intrinsic enzymatic activity of the C-terminal catalytic SET domain of MLL3 and MLL4 is very low (14). Our previous studies showed that the minimal requirements for MLL$_{SET}$ activation are the splA and ryanodine receptor (SPRY) domain of ASH2L (ASH2L$_{SPRY}$, residues 286–505) and a short fragment of RBBP5 (RBBP5$_{AS-ABM}$, residues 330–360) (14). In this work, the MLL3 or MLL4 ternary complex composed of MLL3 or MLL4 SET domain, RBBP5$_{AS-ABM}$, and ASH2L$_{SPRY}$ were purified to >95% homogeneity as previously described (14) (Fig. S1A). The MLL3$_{SET}$-RBBP5$_{AS-ABM}$-ASH2L$_{SPRY}$ and MLL4$_{SET}$-RBBP5$_{AS-ABM}$-ASH2L$_{SPRY}$ were abbreviated as M3RA and M4RA, respectively, throughout this study.

We first used Matrix-Assisted Laser Desorption/Ionization–Time of Flight (MALDI-TOF) mass spectrometry to monitor the methylation progress of H3 20-mer peptides (H3P20) catalyzed by the M3RA and M4RA complexes. For both reactions with 1 μM enzyme, 10 μM H3 peptides, and 250 μM AdoMet, only the monomethylated H3 was observed within 30 min (Fig. S1, *B* and *C*). Therefore, we concluded that the

rates of product formation during steady-state kinetic measurements reflect only the monomethylation activities of M3RA and M4RA. We then used a continuous enzyme-coupled assay to characterize the steady-state kinetic parameters of M3RA and M4RA. In this assay, the cofactor product AdoHcy is rapidly converted into urate and hydrogen peroxide (H_2O_2) in a continuous stepwise enzyme-coupled reaction (Fig. S2). H_2O_2 subsequently reacts with 3,5-dichloro-2-hydroxybenzenesulfonic acid/4-aminophenazone chromogenic system to yield a compound with absorption at 515 nm (A_{515}) (26, 27) (Fig. S2). In terms of these cascading reactions, the accumulation of product AdoHcy can be calculated using the calibration curve generated from AdoHcy standards (Fig. S3*A*).

For M3RA and M4RA-mediated monomethylation reaction, the steady-state kinetic parameters were determined for AdoMet and H3P20, respectively, at fixed concentrations of the other substrate. Representative Michaelis–Menten plots for velocity as a function of AdoMet or H3P20 were shown in Figure 2, *A–D*. At 1600 μM concentration of H3P20, the K_m value for AdoMet with M3RA is 20.0 ± 1.5 μM, with a k_{cat}^{AdoMet} value at 5.0 ± 0.1 min^{-1}. The K_m value for AdoMet with M4RA is 6.9 ± 0.4 μM, with a k_{cat}^{AdoMet} value at 4.8 ± 0.1 min^{-1}. At 200 μM concentration of AdoMet, the K_m value for the H3P20 peptide with M3RA is 586.1 ± 60.5 μM, with a k_{cat}^{H3P20} value at 6.2 ± 0.2 min^{-1}. In comparison, the K_m value for the H3P20 peptide with M4RA is approximately 231.7 ± 17.3 μM, which is less than half of that with M3RA. These kinetic parameters indicate that M4RA has higher affinities for both AdoMet and H3P20 peptides. Since M4RA has similar k_{cat}^{AdoMet} and k_{cat}^{H3P20} as

that of M3RA, thereby smaller K_m values suggest that M4RA bears higher catalytic efficiency (k_{cat}/K_m) than M3RA.

Initial velocity studies suggest a sequential mechanism for M3RA and M4RA

Histone methyltransferases are classical bisubstrate enzymes with histone peptides and AdoMet as the two substrates. Bisubstrate reactions can adopt either a ping-pong or a sequential mechanism, and the latter can be further classified into an ordered or a random sequential mechanism (28). To investigate the exact kinetic mechanisms of MLL3 and MLL4, we first carried out initial velocity studies using the H3P20 peptide that was varied at different fixed concentrations of AdoMet. The resulting Lineweaver–Burk plots show intersecting line patterns for both the M3RA and M4RA complexes and exhibit a decreasing slope with increasing AdoMet concentrations (Fig. 3, *A* and *C*). Similar intersecting lines were also obtained when AdoMet was varied at different fixed H3P20 peptide concentrations (Fig. 3, *B* and *D*). These Lineweaver–Burk plots indicate that MLL3 and MLL4 both catalyze a sequential mechanism in which two substrates bind the enzyme to form a ternary complex before the reaction can take place rather than adopting a ping-pong mechanism.

Secondary plots indicate different sequential mechanisms for M3RA and M4RA

Information derived from our initial velocity studies cannot differentiate between the ordered and random
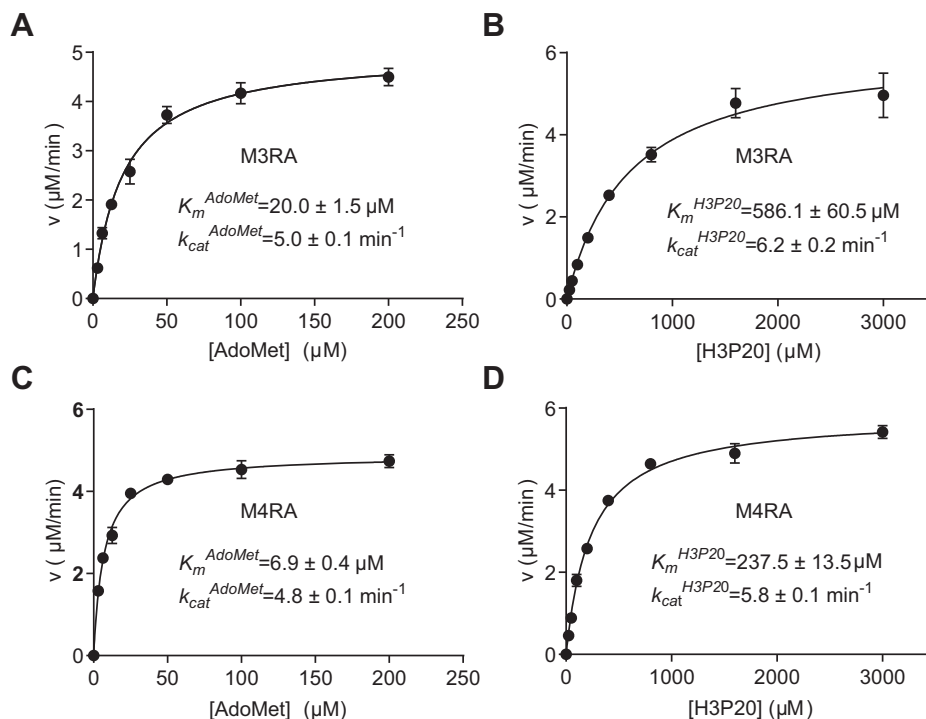
Figure 2. Representative steady-state kinetics of M3RA and M4RA complex. Michaelis–Menten plots for M3RA (*A*) or M4RA (*C*) with varied AdoMet concentrations and fixed H3P20 at 1600 μM; Michaelis–Menten plots for M3RA (*B*) or M4RA (*D*) with varied H3P20 concentrations and fixed AdoMet at 200 μM. *Error bars*, S.D. of three independent measurements.
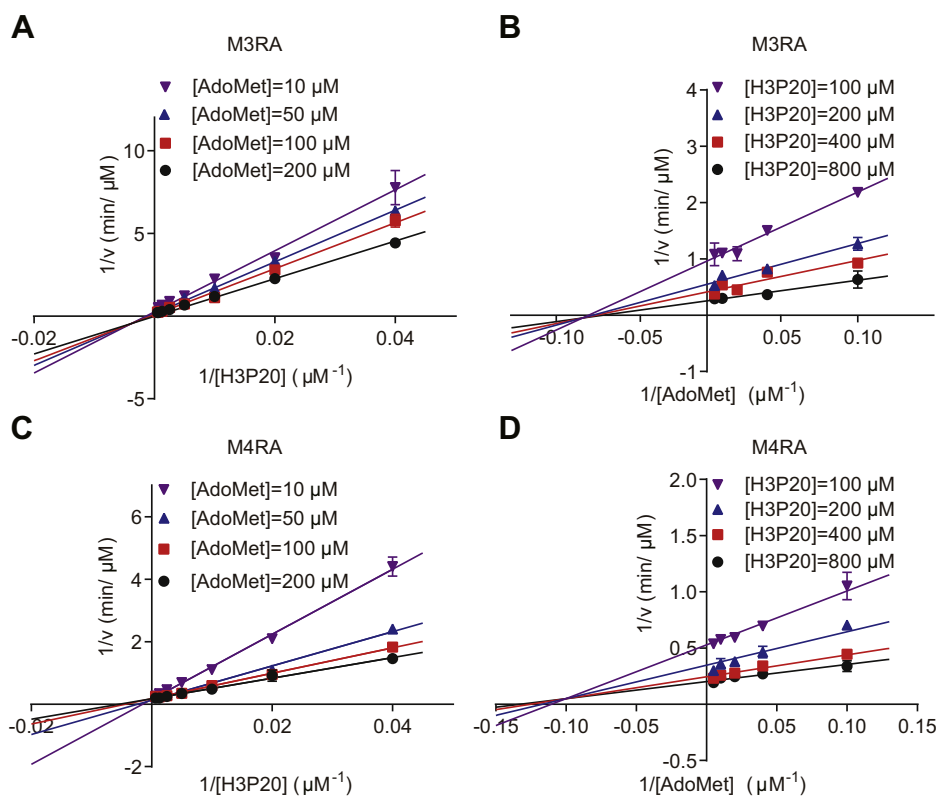
Figure 3. Initial velocity patterns. Lineweaver–Burk plots display an intersecting line pattern, when fixed concentrations of AdoMet were assayed at various concentrations of the H3P20 peptide, for both M3RA (*A*) and M4RA (*C*); Lineweaver–Burk plots display an intersecting line pattern, when fixed concentrations of the H3P20 peptide were assayed at various concentrations of the AdoMet, for both M3RA (*B*) and M4RA (*D*). These intersecting lines are indicative of a sequential mechanism. *Error bars*, S.D. of three independent measurements.

sequential mechanisms. Secondary plots were performed to investigate the exact kinetic mechanism. The rate of reaction for a sequential mechanism can be described by Equation 1. For a random sequential mechanism, Equation 1 can be rearranged to Equation 2, in which K_s^A and K_s^B are the equilibrium dissociation constants for the binary enzyme–substrate complexes EA and EB, respectively; K_{AB} and K_{BA} are the steady-state Michaelis constants (K_m) for the formation of the ternary enzyme–substrate complexes EAB from B to EA and A to EB, respectively, under the assumption of steady state in the concentration of the EAB ternary complex. In Cleland notation (29), A refers to AdoMet, B is the unmethylated H3 peptide, and E is the MLL core complex. Alternatively, Equation 1 can be expressed as Equation 7 in the case of an ordered sequential mechanism. Differentiation between ordered sequential and random sequential mechanisms can be achieved by plotting the apparent Michaelis constants K' and V'_{max} against the concentration of the fixed substrates,

as shown by the distinct stimulation curves in Fig. S4 (28). The concentrations of each substrate and corresponding V'_{max} and K' for each secondary plot are listed in Table S1. The k_{cat}, K_s^A, K_s^B, K_{AB}, and K_{BA} values obtained through nonlinear regression curve fitting by Equations 3–14 are reported in Table 1.

For M3RA-catalyzed reactions, V'_{max} and K' both exhibited a hyperbolic dependence on different fixed H3P20 concentrations (Fig. 4A). Similarly, the V'_{max} and K' also exhibited a hyperbolic dependence on different fixed AdoMet concentrations (Fig. 4B). These hyperbolic patterns reflect the symmetry of the random mechanism, indicating a random sequential mechanism catalyzed by M3RA.

The secondary plots showed a distinct pattern for M4RA-catalyzed reactions. V'_{max} displayed a hyperbolic dependence on different fixed H3P20 concentrations, whereas K' exhibited a decreasing hyperbola curve when the concentration of H3P20 was held at constant (Fig. 4C). On the

Table 1
Kinetic parameters derived from secondary plots

Protein	k_{cat} (min^{-1})	K_s^A (µM)	K_s^B (µM)	K_{AB} (µM)	K_{BA} (µM)
M3RA	6.51 ± 0.47	4.29 ± 0.44	135.72 ± 50.16	659.33 ± 45.66	27.23 ± 3.05
M4RA	6.46 ± 0.32	10.28 ± 0.46	-	147.70 ± 12.52	-

Values reported are the mean ± s.d.
In Cleland notation (29), A refers to AdoMet, B is the unmethylated H3 peptide.
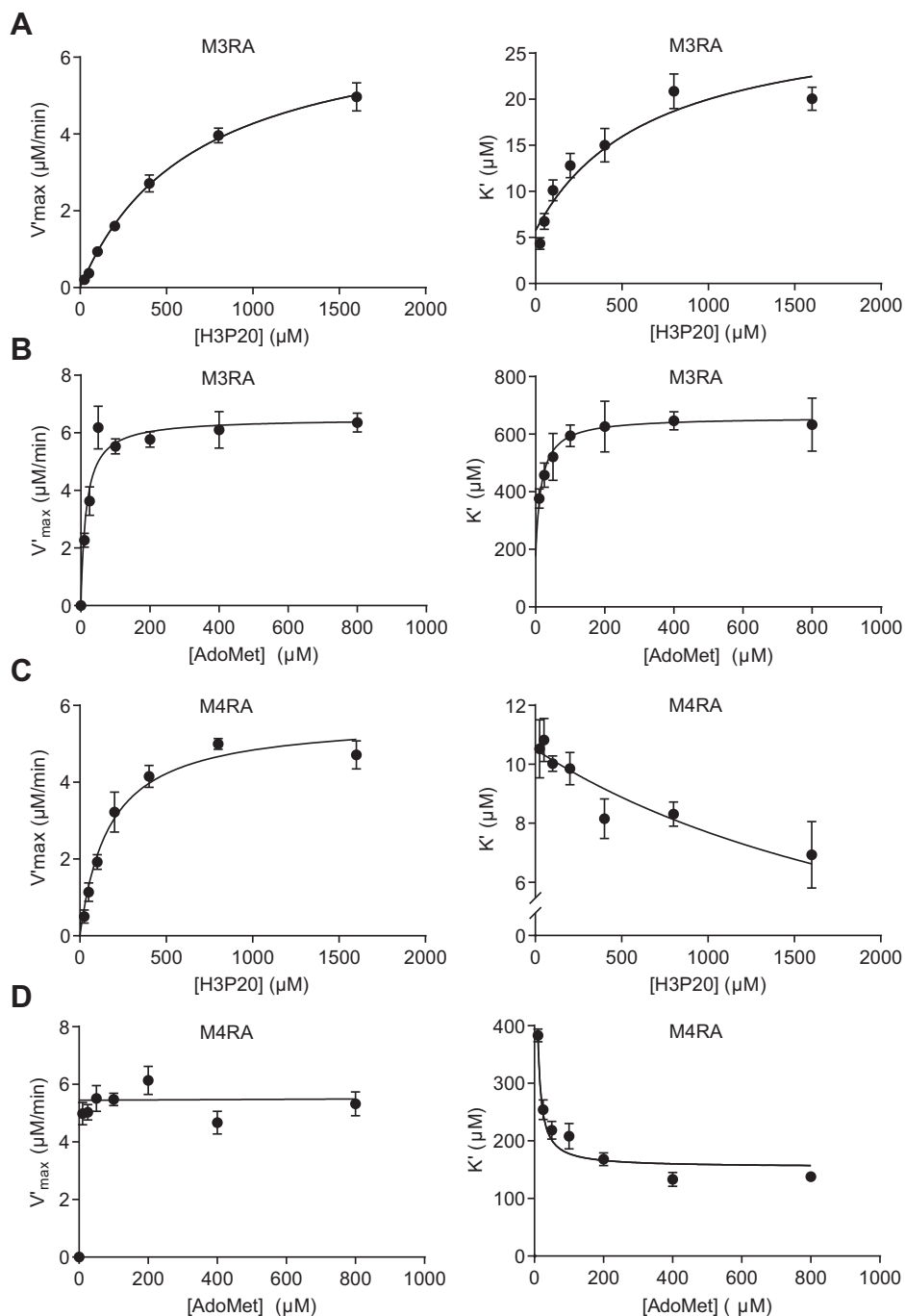
Figure 4. Dependency of the V'_{max} and K' on the concentration of the fixed substrate. For M3RA-catalyzed reactions, V'_{max} and K' both display a hyperbolic dependence on the concentration of the H3P20 peptide (*A*) or AdoMet (*B*), indicative of a random-sequential mechanism; For M4RA-catalyzed reactions, V'_{max} and K' both exhibit a hyperbolic dependence on the concentration of the H3P20 peptide (*C*); K' exhibits a hyperbolic dependence on the concentration of AdoMet while V'_{max} is nearly independent of the concentration of AdoMet (*D*), indicative of a ordered-sequential mechanism in which AdoMet binds first. *Error bars*, S.D. of three independent measurements.

other hand, K' displayed a decreasing hyperbola curve, while V'_{max} was roughly kept constant at different fixed concentrations of AdoMet (Fig. 4*D*). These secondary plot results imply that M4RA may act in an ordered sequential mechanism in a methyl transfer reaction. Additionally, V'_{max} is independent of the concentration of AdoMet, suggesting that AdoMet is the first substrate binding to M4RA in the ordered-sequential reaction.

Inhibition studies confirm the kinetic mechanism difference between MLL3 and MLL4

The secondary plot analyses revealed the distinct kinetic mechanisms of MLL3 and MLL4: MLL3 adopts a random sequential mechanism, and MLL4 utilizes an ordered sequential mechanism. These two kinetic mechanisms both have well-established and characteristic dead-end inhibition (see Table S2) (30) and product inhibition patterns (see

Table S3) (31). Based on that, we carried out these inhibition studies and analyzed our inhibition data to determine which mechanism is best supported by our results.

First, we carried out dead-end analogue inhibition studies using two inhibitors: H3P20K4Ac and sinefungin. H3P20K4Ac is almost identical to H3P20 except that the K4 residue is acetylated, so H3P20K4Ac can no longer act as a methyl acceptor. Sinefungin is analogous to the cofactor

AdoMet, in which the δ-amine and methylene moieties replace the methyl group and sulfonium cation in AdoMet, respectively. In these inhibition studies, the concentration of one substrate was held constant, while the concentrations of the other substrate and the inhibitors were varied as described in the Experimental procedures. Data were interpreted by both linear and nonlinear analyses. Lineweaver–Burk plots were generated according to the Equation 15 to
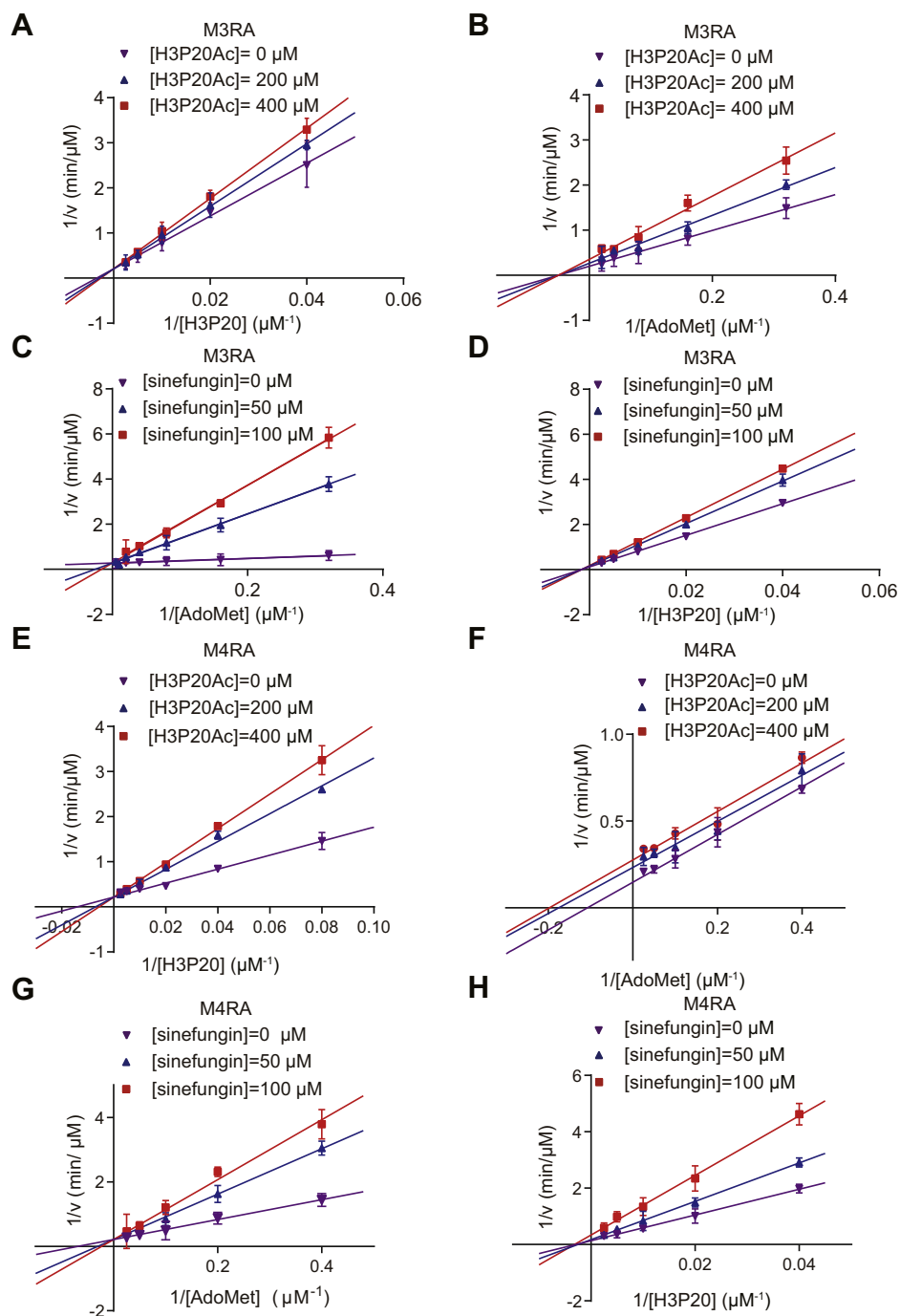
Figure 5. Dead-end analogue inhibition studies with H3P20Ac and sinefungin. For M3RA-catalyzed reactions, H3P20Ac acts as a competitive inhibitor against the H3P20 peptide (*A*) and a noncompetitive inhibitor against AdoMet (*B*); Sinefungin serves as a competitive inhibitor against AdoMet (*C*) and a noncompetitive inhibitor against the H3P20 peptide (*D*); For M4RA-catalyzed reactions, H3P20Ac works as a competitive inhibitor against the H3P20 peptide (*E*) and an uncompetitive inhibitor against AdoMet (*F*); Sinefungin acts as a competitive inhibitor against AdoMet (*G*) and a noncompetitive inhibitor against the H3P20 peptide (*H*). *Error bars*, S.D. of three independent measurements.

visualize data and estimated the inhibition patterns. The Lineweaver–Burk plots obtained at different inhibitor concentrations can indicate the mode of inhibition: if the lines converge on the y-axis, it is competitive inhibition; they converge on the x-axis for noncompetitive inhibition; and parallel lines for uncompetitive inhibition (31). For nonlinear analyses, each data set was fit to equations corresponding to competitive (Equation 16), noncompetitive (Equation 17), and uncompetitive (Equation 18) inhibition. Representative nonlinear curves were shown in Fig. S5. Data sets were assessed as best fitting to models based on the best coefficient of determination and the lowest standard errors of the estimate listed in Table S4 to reinforce the conclusions from linear analyses.
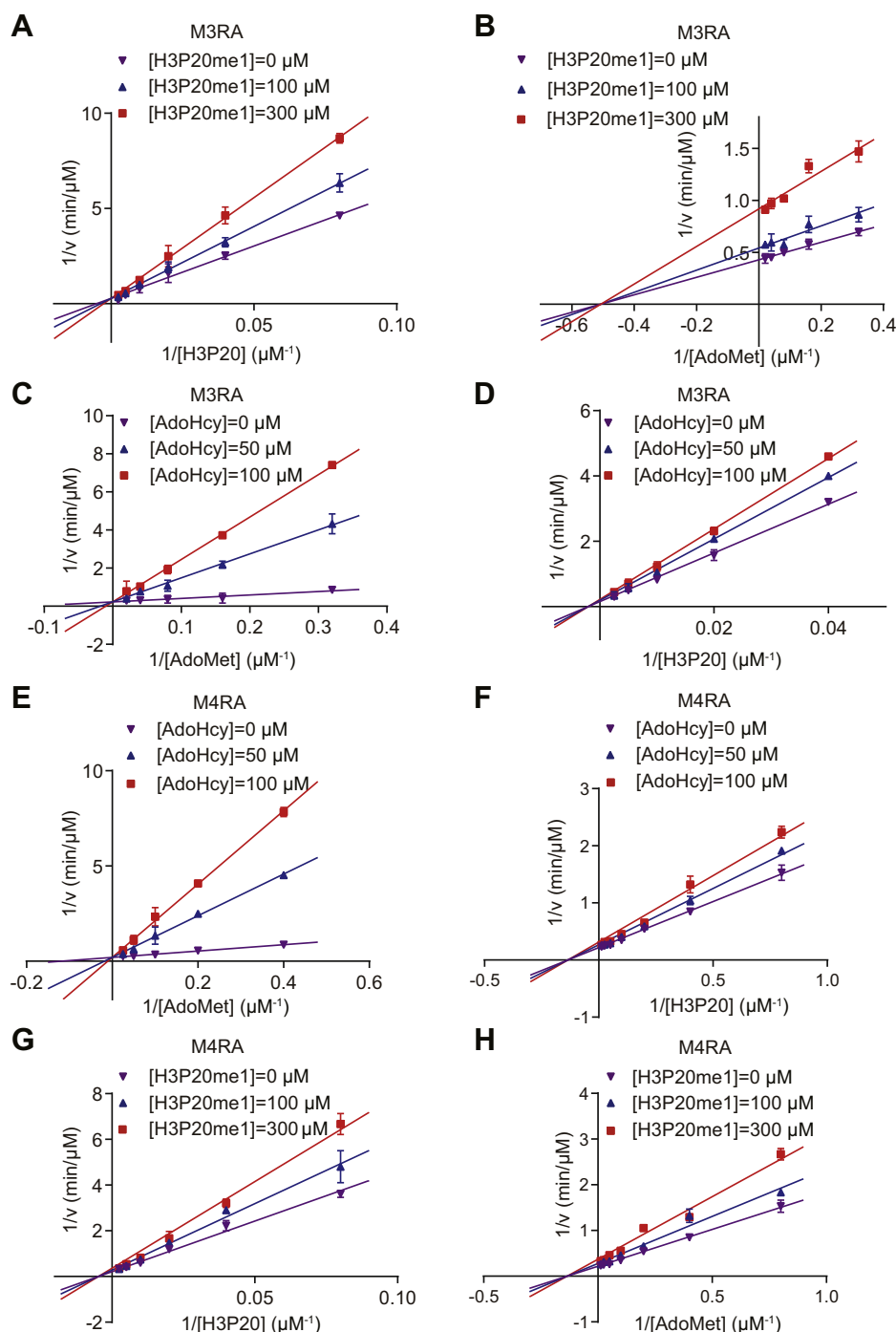
Figure 6. Product inhibition studies with AdHcy and H3P20me1. For M3RA-catalyzed reactions, H3P20me1 acts as a competitive inhibitor against the H3P20 peptide (*A*) and a noncompetitive inhibitor against AdoMet (*B*); AdoHcy serves as a competitive inhibitor against AdoMet (*C*) and a noncompetitive inhibitor against the H3P20 peptide (*D*); For M4RA-catalyzed reactions, AdoHcy works as a competitive inhibitor against AdoMet peptide (*E*) and a noncompetitive inhibitor against the H3P20 peptide (*F*). H3P20me1 acts as noncompetitive inhibitors against both H3P20 (*G*) and AdoMet (*H*); *Error bars*, S.D. of three independent measurements.

Kinetic mechanisms of MLL3 and MLL4 complexes

For M3RA-catalyzed reactions, the results showed that H3P20Ac acted as a competitive inhibitor when the concentration of H3P20 was varied and AdoMet concentration was held constant, indicating that H3P20Ac competes with H3P20 for the same form of M3RA (Fig. 5A). In contrast, the inhibition by H3P20Ac was noncompetitive when AdoMet was the variable substrate (Fig. 5B), indicating that H3P20, as well as its competitive inhibitor H3P20Ac, can bind to the free M3RA and M3RA-AdoMet binary complex indiscriminately. Similarly, sinefungin acted as a competitive inhibitor when AdoMet concentration was variable and as a noncompetitive inhibitor when H3P20 concentration was variable (Fig. 5, C and D), which is in accordance with the symmetry of the random sequential mechanism. Thus, we speculated that there is no particular order in the sequential binding of substrates H3P20 or AdoMet to the M3RA to form the ternary complex, which can be identified as the random sequential mechanism.

The same set of experiments on M4RA suggested that H3P20Ac acted as a competitive inhibitor when H3P20 was the variable substrate (Fig. 5E), and sinefungin was competitive when AdoMet was the variable substrate (Fig. 5G). Sinefungin showed a noncompetitive inhibition pattern when H3P20 was the variable substrate (Fig. 5H). However, parallel lines in Figure 5F suggested that H3P20Ac was an uncompetitive inhibitor when AdoMet was the variable substrate, implying that H3P20Ac and its analogue substrate H3P20 only bind to the M4RA-AdoMet binary complex but not M4RA enzyme alone. Taken together, these results are consistent with an ordered sequential mechanism in which AdoMet binds to the enzyme complex first.

To further validate the kinetic models and determine the release order of products, we performed product inhibition studies with H3P20me1 (monomethylated on K4) and AdoHcy. For the AdoHcy inhibition experiments, a different MALDI-TOF-based assay was used as described in the Experimental procedures. The kinetic mechanism was estimated by comparing the inhibition patterns with the diagnostic patterns listed in Table S3.

For M3RA-catalyzed reactions, H3P20me1 was a competitive inhibitor when the concentration of H3P20 was varied and AdoMet concentration was held constant (Fig. 6A) and a noncompetitive inhibitor when AdoMet was the variable substrate (Fig. 6B). AdoHcy acted as a competitive inhibitor when AdoMet was the variable substrate (Fig. 6C) and a noncompetitive inhibitor when H3P20 was variable (Fig. 6D). The noncompetitive inhibition patterns provide strong evidence that M3RA can form AdoMet-M3RA-H3P20me1 and H3P20-M3RA-AdoHcy dead-end complex. Therefore, these results are consistent with the rapid equilibrium random sequential mechanism with dead-end EAP and EBQ (Table S3).

The same product inhibition experiments were performed for M4RA-catalyzed reactions. AdoHcy acted as a competitive inhibitor when AdoMet was variable (Fig. 6E) and noncompetitive inhibitor when H3P20 was variable (Fig. 6F), indicating that AdoHcy competes with AdoMet for the same form of M4RA. The above dead-end analogue inhibition studies

suggested that AdoMet is the first substrate to bind to the free M4RA; therefore the ability of AdoHcy to bind apo M4RA indicates that it is the last product released from M4RA to renew the enzyme. Notably, when H3P20 was variable, H3P20me1 acted as a noncompetitive inhibitor (Fig. 6G), indicating that H3P20me1 was unable to bind the same form of M4RA as H3P20 (i.e., neither free M4RA nor M4RA-AdoMet). These inhibition patterns clearly rule out a random sequential mechanism for M4RA and instead suggest that M4RA utilizes a steady-state ordered sequential mechanism in which AdoMet binds to the enzyme prior to the H3 peptide and the methylated H3 peptide dissociates from the enzyme before AdoHcy detaches after methylation. The observation that H3P20me1 acted as a noncompetitive inhibitor for AdoMet (Fig. 6H) is consistent with this mechanism.

Taken together, the dead-end analogue and product inhibition patterns obtained for AdoMet and H3P20 (listed in Tables 2 and 3) demonstrate that M3RA and M4RA adopt two different sequential kinetic mechanisms (Fig. S6).

M3RA and M4RA exhibit diverse histone-binding property

The different sequential kinetic mechanism suggests that M3RA and M4RA may have distinct substrate binding properties. We first use Isothermal Titration Calorimetry (ITC) assays to assess the interaction between AdoMet and M3RA/M4RA. M3RA and M4RA bound AdoMet with similar dissociation constant (Kd) values and enthalpy changes (Fig. 7A), indicating that the different kinetic mechanism is not derived from the differential cofactor-binding ability of M3RA and M4RA.

We then evaluated the H3 peptide-binding ability of M3RA and M4RA by FP assays. Because the binding affinity between wild-type H3 peptide and M3RA/M4RA is too weak to be detected by FP assays (not shown), we used a mutated H3P20 peptide (H3K4M), which contains a methionine in the K4 position. K-to-M mutations have been widely proven to increase the binding between histone peptides and SET domains (32). As shown in Figure 7B, M3RA had a strong binding with H3K4M peptide (Kd around 14 μM). In the presence of AdoMet, the binding affinity between H3K4M and M3RA was enhanced around threefold (Fig. 7B). AdoHcy had no effect on the M3RA-H3K4M interaction. It indicates that M3RA can bind H3 peptide independent of AdoMet binding, consistent with the random sequential kinetic model of M3RA.

In sharp contrast, M4RA has no detectable interaction with H3K4M in the absence of AdoMet (Fig. 7C). The cofactor AdoMet, but not AdoHcy, greatly bursts the interaction between M4RA and H3K4M (Fig. 7C). This histone-binding property of M4RA confirms that AdoMet binding is a prerequisite for H3 peptide binding with M4RA, supporting the ordered sequential kinetic model of M4RA in which the cofactor AdoMet binds to the enzyme prior to the H3 peptide.

Molecular dynamic simulations highlight the importance of conformational dynamics in differentiating MLL3 and MLL4

To explain why M3RA and M4RA adopt different sequential kinetic mechanisms and histone-binding properties, we

Table 2
Dead-end analogue inhibition pattern

Protein	Dead-end analogue	Varied substrate	Inhibition pattern
M3RA	Sinefungin	AdoMet	Competitive
		H3P20	Noncompetitive
	H3P20Ac	H3P20	Competitive
		AdoMet	Noncompetitive
M4RA	Sinefungin	AdoMet	Competitive
		H3P20	Noncompetitive
	H3P20Ac	H3P20	Competitive
		AdoMet	Uncompetitive

investigated the potential structural difference between M3RA and M4RA. We previously solved the structure of M3RA in complex with AdoHcy and H3 (14). The structure of M4RA in complex with AdoMet and H3 was modeled from the M3RA complex (PDB:5F6K) and MLL4$_{SET}$ (PDB: 4Z4P). In these two complex structures, MLL3$_{SET}$ and MLL4$_{SET}$ showed similar conformations (Fig. 8*A*) and could be superimposed with a root mean square deviation (RMSD) value of 1.13 Å for 148 equivalent Cα atoms. The main conformational differences between MLL3$_{SET}$ and MLL4$_{SET}$ were observed in the loop regions, and the most divergent region is the Post-SET motif (loop 6) (Fig. 8*A*). In these complex structures, MLL3$_{SET}$ and MLL4$_{SET}$ have almost identical binding interfaces for AdoMet and H3K4 (Fig. 8, *B* and *C*).

We reason that although the M3RA and M4RA share similar active conformations in the final methyl-transfer step, they may have different conformational dynamics in the whole catalytic process. To provide the insights into the dynamic change of M3RA and M4RA upon the cofactor binding, we performed all-atom molecular dynamics simulation. Four groups, namely M3RA with and without AdoMet and M4RA with and without AdoMet, were simulated in CHARMM36 force field for 100 ns as described in Experimental procedures.

To compare the effect of AdoMet binding to the overall dynamics of the SET domains of MLL3 and MLL4 in M3RA and M4RA complexes, we calculated the root mean square fluctuation (RMSF) values of the Cα of each residue. We found that M3RA and M3RA+AdoMet have similar RMSF plots (Fig. 8*D*), which indicates that MLL3$_{SET}$ does not undergo dramatic conformational change upon AdoMet binding. In sharp contrast, the RMSF values of MLL4$_{SET}$ are significantly reduced by the binding of AdoMet (Fig. 8*E*), suggesting an overall structural stabilization effect of AdoMet on MLL4$_{SET}$. Notably, the fluctuations of four flexible loop regions, which comprise the AdoMet-binding pocket (loop 1, 2, 4, and 6 in

Table 3
Product inhibition pattern

Protein	Product inhibitor	Varied substrate	Inhibition pattern
M3RA	AdoHcy	AdoMet	Competitive
		H3P20	Noncompetitive
	H3P20me1	H3P20	Competitive
		AdoMet	Noncompetitive
M4RA	AdoHcy	AdoMet	Competitive
		H3P20	Noncompetitive
	H3P20me1	H3P20	Noncompetitive
		AdoMet	Noncompetitive

Fig. 8*A*), were mostly suppressed in the presence of AdoMet (Fig. 8*E*), indicating that AdoMet binding can significantly stabilize the inherently dynamic AdoMet-binding pocket of MLL4$_{SET}$. Additionally, we also calculated the free energy landscape of the four groups. We found that AdoMet can almost completely alter the free energy landscape of M4RA but slightly shift the free energy landscape of M3RA (Fig. S7).

To further probe the dynamics of histone-binding pocket upon AdoMet binding, we examined the fluctuation of the K4-binding pocket represented by the distance between Cα atoms of V4824 and Y4883 in MLL3 and I5450 and Y5510 in MLL4. We found that the dynamics of M3RA substrate-binding pocket is independent of AdoMet as shown by the similar trend of the width of the K4-binding pocket in M3RA with and without AdoMet (Fig. 8*F*). On the contrary, we found that the K4-binding pocket in M4RA alone ranges from 10 Å to 16 Å, which is more dynamic than M3RA. In the presence of Ado-Met, the fluctuation of the K4-binding pocket in M4RA is obviously decreased, generating a more stable environment in favor of K4 binding (Fig. 8*G*).

Summing up all the data above, we conclude that M4RA alone might be over dynamic for H3 binding, and AdoMet-induced conformational constraints on the AdoMet-binding pocket and H3 substrate-binding pocket could stabilize the specific conformation, which facilitates substrate H3 entry in both M3RA and M4RA but to a greater extend in M4RA.

Discussion

A detailed characterization of histone methyltransferases is essential for understanding their biological functions. The present study represents a comprehensive kinetic analysis of KMT2-family methyltransferases that determines all kinetic parameters and reveals the different kinetic mechanisms between MLL3 and MLL4. MLL3 functions in a random sequential bi–bi mechanism while MLL4 utilizes an ordered sequential bi–bi mechanism. The distinct kinetic mechanisms stem from the different dynamic nature of MLL3 and MLL4. The AdoMet and histone-binding pockets in MLL3 are relatively stable and competent for substrate binding. Thus MLL3 can bind AdoMet and histone independently, consistent with the random sequential mechanism. In constrast, the histone-binding pocket in MLL4 is more dynamic than that of MLL3, which prevents histone binding with MLL4 in the absence of AdoMet. AdoMet binding can restrict the fluctuation of the active site and maintain a conformation ready for histone recognition, thus explaining why MLL4 adopts an ordered sequential mechanism in which AdoMet binds to the enzyme prior to H3.

It should be noted that both the ordered sequential mechanism and random sequential mechanism have been reported in different SET-containing methyltransferases. SET7/9, which catalyzes the monomethylation on histone H3K4, adopts an ordered sequential mechanism with AdoMet binding first (33). Previous studies also suggested that AdoMet binding triggered the folding and stabilization of the SET7/9 post-SET loop to form an efficient substrate-binding groove for substrate

recognition ([34](#)), in a similar fashion as M4RA. On the other hand, G9a, SUV39H1, and SETD2 all catalyze methylation reactions through a random sequential mechanism like M3RA ([35–37](#)). We hypothesize that the dynamic properties of substrate-binding pockets of SET domains determine the catalytic pathways: the SET domains with a relatively stable active site adopt a random sequential mechanism, while the SET domains with a dynamic active site utilize an ordered sequential mechanism because they need AdoMet-binding to stabilize the active site for subsequent histone binding. The dynamic nature and kinetic mechanisms of other SET-domain methyltransferases merit further studies to generalize our model.

In the present studies, we used the minimized M3RA and M4RA complexes to characterize their methylation activity toward histone peptides. Our steady-state kinetic parameters of M3RA and M4RA are similar as that of MLL4-WDR5-ASH2L-RBBP5-DPY30 (M4WARD) complex (k_m^{H3P20} is 107 ± 16 µM and k_{cat}^{H3P20} is 2.65 ± 0.11 min^{-1}) determined by Wilson lab ([25](#)), suggesting that the data from the minimized complexes could also apply to the pentameric MLL3 and MLL4 complexes. At this stage, we cannot rule out the possibility that the MLL3 or MLL4 complex may adopt different kinetic mechanisms when catalyzing methylation of nucleosomes, which is currently under investigation.

MLL4 plays a more important role than MLL3 during ESC differentiation ([20](#)). Previous results also indicate that MLL4 is the dominant monomethyltransferase on enhancers. Three features of MLL4 may contribute to its dominant roles. First, MLL4 has a higher catalytic efficiency (k_{cat}/K_m) than MLL3 ([Fig. 2](#)), thereby ensuring fast enhancer priming. Second, the catalytic turnover rate $\left(V_{max}^{'}\right)$ of MLL4 is less affected by the variation of AdoMet concentration ([Fig. 4D](#)). Third, the Ki value of AdoHcy for MLL3 is threefold lower than that of MLL4 ([Fig. 6](#), *C* and *E* and [Table S4](#), 11.22 µM *versus* 4.19 µM), indicating that AdoHcy inhibits MLL3 activity more efficiently than MLL4. The latter two features make MLL4 activity less affected by changes in the ratio of Ado-Met/AdoHcy (also termed methylation potential (MP)) than MLL3. MP is a tissue-specific and metabolism-specific methylation indicator that is influenced by a variety of factors such as diet ([38](#)), hypoxia ([39](#)), development stages ([38](#)), and pathological conditions ([40, 41](#)). Thus, perturbations of MP during the embryonic development may greatly interfere with MLL3 activity but only moderately affect MLL4 activity. Consequently, MLL4, but not MLL3, ensures stable and efficient methyltransferase activity that is required for enhancer activation and gene expression during cell fate transition. Thus, our characterization of the catalytic differences between MLL3 and MLL4 may shed light on the differential requirements of MLL3 and MLL4 during ESC differentiation.

Recent massive parallel sequencing of cancer exomes revealed extensive somatic mutations in KMT2-family members, especially in *Mll3* and *Mll4*. *Mll3* and *Mll4* are the most frequently mutated genes in human cancers, and their variants have been reported in a variety of malignancies including non-Hodgkin's lymphoma, colorectal cancer, lung cancer, breast cancer, bladder cancer, and prostate cancer ([42](#)). Accordingly, MLL3 and MLL4 are envisioned as the potential therapeutic targets for the future treatment of multiple cancers. To date, there is no selective inhibitor against MLL3 or MLL4. Our results reveal distinct kinetic mechanisms of MLL3 and MLL4 and associated dynamic transitions, which provide an inspiration on selective inhibitor development.

The kinetic mechanism and conformational plasticity of the catalytic domain have been exploited to direct the development of specific inhibitors of several methyl-transferases such as SET7/9, PRMT5, DOT1L, and EZH2 ([43](#)). SET7/9 selective inhibitor (R)-PFI-2 and PRMT5 selective inhibitor EPZ015666 both bind to the substrate-binding pocket only in the presence of AdoMet and make direct interactions with the departing methyl group of AdoMet ([44, 45](#)). These unconventional inhibitors enlighten us that a cofactor-dependent inhibitor can be designed to suppress the activity of MLL4 more effectively than MLL3. Furthermore, the AdoMet-binding groove and surrounding broad surfaces of MLL3 and MLL4 exhibit different dynamic properties and have the potential to become a target for specific inhibitor development. The clinical DOT1L inhibitor pinometostat (EPZ-5676), a distant analog of AdoMet, occupies a cavity juxtaposed to the AdoMet-binding site and locks DOT1L in an inactive conformation by restricting a conformationally dynamic activation loop in a catalytically incompetent state ([43](#)). Similar strategies can be exploited to design a specific inhibitor or activator targeted MLL3 or MLL4 specifically. For instance, elaborately designed allo-steric compounds that only bind to the dynamic pocket of MLL4 and lock MLL4 in the inactive or active state might have the potential to serve as the MLL4-specific inhibitors or activators without altering the activity of MLL3. These inhibitors can also act as powerful tools to explore the specific functions of MLL3 and MLL4 *in vivo* and ultimately benefit the therapies development of MLL4-associated diseases in the future.

Experimental procedures

Protein purification

The SET domains of MLL family proteins, the SPRY domain of ASH2L, the AS-ABM truncation of RBBP5, and the H3P20 peptide (derived from histone H3 1–20 amino acids with an additional tyrosine at the C-terminus, which helps UV quantification), were purified as described before ([14](#)). *Escherichia coli* Rosetta (DE3) bearing pET28b expression plasmids were induced with 0.1 mM isopropyl 1-thio-β-D-galactopyranoside (IPTG) in LB media with 100 µg/ml kanamycin. MLL$_{SET}$, ASH2L$_{SPRY}$, and RBBP5$_{AS-ARM}$ were induced at 16 °C for 16 h, and H3P20 was expressed at 37 °C for 4 h. Cells were harvested by centrifugation at 4000g for 10 min and lysed by sonication in lysis buffer (50 mM Tris-HCl, pH 8.0, 400 mM NaCl, 10% glycerol, 2 mM 2-mercaptoethanol, and protease inhibitors cocktail). Lysates were clarified by
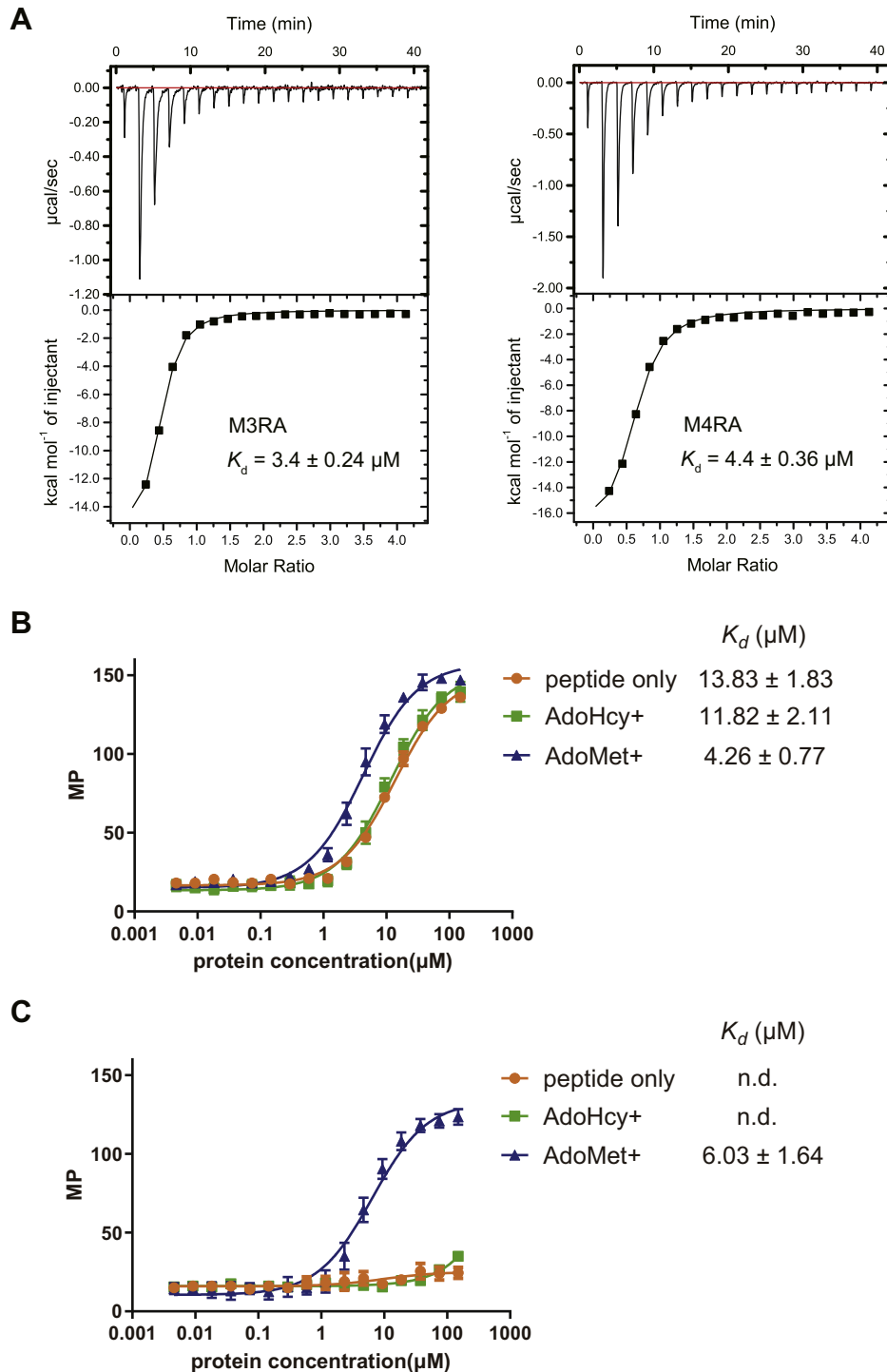
Figure 7. M3RA and M4RA exhibit distinct H3 peptide binding properties. *A*, Isothermal Titration Calorimetry (ITC) analyses of AdoMet binding to M3RA and M4RA complexes. M3RA (*left*) and M4RA (*right*) bound AdoMet with similar dissociation constant (Kd) values and enthalpy changes. *B*, fluorescence polarization analysis of H3K4M peptide binding to M3RA complex. M3RA binds H3K4M with a Kd of 13.83 ± 1.83 μM. Inclusion of AdoHcy does not promote K4M peptide binding. Inclusion of AdoMet results in a slight affinity promotion with a Kd of 4.26 ± 0.77 μM. *C*, fluorescence polarization analysis of H3K4M peptide binding to M4RA complex. M4RA alone does not bind K4M peptide. Addition of AdoMet causes potent K4M binding with a Kd of 6.03 ± 1.64.

ultracentrifugation at 10,000g for 50 min, and supernatants were purified using Ni-NTA beads (Qiagen). Bound proteins were digested by ULP1 for 5 h to remove the sumo tag and further purified on Hiload Superdex75 gel filtration chromatography except for the H3P20 peptide. The gel filtration buffer for MLL$_{SET}$ contains 25 mM Tris-HCl, 300 mM NaCl, and 10% glycerol, pH 8.0; for copurified binary complex RBBP5$_{AS-ABM}$-ASH2L$_{SPRY}$ contains 25 mM Tris-HCl, 150 mM NaCl, pH 8.0. The purified proteins were concentrated, and aliquots were stored at −80 °C. The MLL$_{SET}$-RBBP5$_{AS-ABM}$-

Kinetic mechanisms of MLL3 and MLL4 complexes

ASH2L$_{SPRY}$ complex was obtained by mixing RBBP5$_{AS-ABM}$-ASH2L$_{SPRY}$ and MLL$_{SET}$ and separating on Hiload Superdex75 with buffer containing 25 mM Tris-HCl, 150 mM NaCl, pH 8.0. The H3P20 peptide was separated on Hiload Superdex30 with 150 mM NH$_4$HCO$_3$. The peptide-containing fractions were freeze-dried, and the powders were stored at –20 °C.

Mass-spectrometry-based methylation assay

The peptide methylation progression catalyzed by M3RA or M4RA was monitored by MALDI-TOF Mass Spectrometry. In total, 250 µM AdoMet and 10 µM H3P20 peptide were pre-incubated in MS buffer (20 mM HEPES, 10 mM NaCl, 5 mM DTT, pH 7.8) for 15 min at 25 °C. The reaction was initiated by adding 1 µM M3RA or M4RA at 25 °C and quenched at various appropriate times by adding trifluoroacetate (TFA) to a final concentration of 0.5% and cooling at 4 °C. Reaction samples were mixed with 10 mg/ml α-cyano-4-hydroxy cinnamic acid (CHCA) in 50% acetonitrile, 50% water, and 0.1% TFA, and spotted onto MALDI plate. The molecular mass was measured on MALDI-TOF (AB SCIEX TOF/TOF 5800). Final spectra were the average of 200 shots per position at 200 different positions on each spot. The percentage of the methylated H3P20 peptide was calculated as previously described (14).

Continuous enzyme-coupled methylation assay

To study the kinetic mechanisms of M3RA and M4RA, a continuous enzyme-coupled spectrophotometric assay that monitors the generation of AdoHcy was established. M3RA and M4RA activities were measured under the following conditions in a final volume of 100 µl: 25 mM Tris-HCl (pH8.0), 320 nM AdoHcy Nucleosidases, 480 nM Adenine Deaminase, 40 U/l Xanthine Oxidase, 20,000 U/l Horseradish peroxidase, 4.5 mM 3,5-dicholoro-2-hydroxybenzenesulfonic acid, 0.894 mM 4-aminophenazone, 40 µM MnCl$_2$, and 2.25 µM K$_4$Fe(CN)$_6$·3H$_2$O. Excessive coupling enzymes and chromogenic reagents were used to ensure that methylation catalyzed by MAR was the rate-limiting step in the coupled assay. For different assays, H3P20 peptide concentrations were varied from 0 to 1600 µM and AdoMet concentrations were varied from 0 to 400 µM as indicated. All components except enzyme were initially mixed in a microvolume cuvette at 30 °C, and the reactions were initiated by adding 1 µM M3RA or M4RA. To eliminate the effect of inherent AdoHcy contamination in commercial AdoMet, we use high-purity AdoMet (purity ≥ 95%, CAYMAN, Item No.13956) and let the trace AdoHcy firstly react with the chromogenic system for 5 min to be consumed up before we start the methylation reaction. This step ensured that any subsequent change in absorbance at 515 nm all resulted from the methylation reaction (Fig. S3B). Absorbance at 515 nm was monitored using Biomate 3S UV-Visible Spectrophotometer (Thermo Fisher) for 15 min at 30 °C. Steady-state kinetic paramet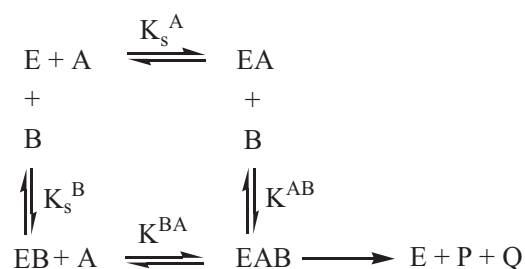ers were obtained by fitting the initial rates to Michaelis–Menten equation (Equation 1) using nonlinear regression in GraphPad Prism 8 software.

Initial velocity study

Using AdoMet (200 µM) and H3P20 (400 µM) as substrates, the methylation velocity has a linear dependence on the enzyme concentration in the range of 0 to 4 µM (Fig. S3, C and D), highlighting that the methylation reaction is the rate-limiting step in the coupled assay. We chose 1 µM enzyme to get the best signal intensity of the methylation reaction. At such an enzyme concentration, the initial linear phase lasts for at least 6 min with less than 5% of potential sites methylated (Fig. S3, E and F). Thereafter, the initial velocity was determined from the data within the first 5 min. The initial rates for the H3P20 peptide were examined at different concentrations of AdoMet (0, 3.125, 6.25, 12.5, 50, 100, and 200 µM). The initial rates for AdoMet were obtained at different concentrations of the H3P20 peptide (0, 25, 50, 100, 200, 400, 800, 1600, and 3000 µM). Lineweaver–Burk plots were used to evaluate the reaction kinetic mechanisms.The apparent V_{max} (V'_{max}) and K_m (K') were determined by fitting a series of initial rate using Michaelis–Menten equation (Equation 1) with GraphPad Prism 8.

Secondary plot analysis

Irrespective of the scheme of reaction, all bisubstrate reactions obey the Michaelis–Menten equation (Equation 1). A general scheme for a random sequential bi–bi mechanism reaction is

$$
\begin{array}{ccc}
E + A & \xrightleftharpoons{K_s^A} & EA \\
+ & & + \\
B & & B \\
\Big\Updownarrow K_s^B & & \Big\Updownarrow K^{AB} \\
EB + A & \xrightarrow{K^{BA}} & EAB \longrightarrow E + P + Q
\end{array}
$$

Under the assumption that rapid equilibrium binding of either substrate A or B to the free enzyme and equilibrium binding of A to EB and B to EA, or the steady-state in the concentration of the EAB ternary complex, the rate equation for scheme 1 is described by Equation 2 (28, 46), which can be rearranged into hyperbolic forms with respect to A or B to obtain Equations 3–6 (28).

A general scheme for an ordered sequential bi–bi mechanism reaction is

$$
E + A \xrightleftharpoons{K_s^A} EA + B \xrightleftharpoons{K^{AB}} EAB \longrightarrow E + P + Q
$$

Under the assumption that rapid equilibrium binding substrate A to the free enzyme and equilibrium binding of B to EA, or the steady-state in the concentration of the EAB ternary complex, the rate equation for scheme 1 is described by

Equation 8 (28, 46), which can be rearranged into hyperbolic forms with respect to A or B to obtain Equations 9–12 (28).

$$\frac{v}{V'_{max}} = \frac{[S]}{K' + [S]} \tag{1}$$

$$\frac{v}{V_{max}} = \frac{[A][B]}{K_s^A K^{AB} + K^{AB}[A] + K^{BA}[B] + [A][B]} \tag{2}$$

$$V'_{max} = \frac{V_{max}[A]}{K^{BA} + [A]} \tag{3}$$

$$K' = \frac{K^{AB}\left(K_s^A + [A]\right)}{K^{BA} + [A]} \tag{4}$$

$$V'_{max} = \frac{V_{max}[B]}{K^{AB} + [B]} \tag{5}$$

$$K' = \frac{K^{BA}\left(K_s^B + [B]\right)}{K^{AB} + [B]} \tag{6}$$

$$k_{cat} = \frac{V_{max}}{[E]} \tag{7}$$

$$\frac{v}{V_{max}} = \frac{[A][B]}{K_s^A K^{AB} + K^{AB}[A] + [A][B]} \tag{8}$$

$$V'_{max} = \frac{V_{max}[B]}{K^{AB} + [B]} \tag{9}$$

$$K' = \frac{K_s^A K^{AB}}{K^{AB} + [B]} \tag{10}$$

$$V'_{max} = V_{max} \tag{11}$$

$$K' = \frac{K_s^A K^{AB}}{[A]} + K^{AB} \tag{12}$$

$$K_s^A = \frac{K_s^B K^{BA}}{K^{AB}} \tag{13}$$

$$K_s^B = \frac{K_s^A K^{AB}}{K^{BA}} \tag{14}$$

According to the Equations 3–6 and 9–12, differentiation between ordered sequential and random sequential mechanisms can be achieved by scrutinizing the dependency of V'_{max} and K' on substrate A and B, respectively, in secondary plots. For the secondary plot *versus* AdoMet, constant (0, 12.5, 25, 50, 100, 200, 400, 800 μM) AdoMet and variable (0, 25, 50, 100, 200, 400, 800, 1600 μM) H3P20 were used and the V'_{max} and K' at different fixed concentrations of substrate AdoMet were derived from the initial velocity studies. For the secondary plot *versus* H3P20, constant (0, 25, 50, 100, 200, 400, 800, 1600 μM) H3P20 and variable (0, 6.25, 12.5, 25, 50, 100, 200 μM) Ado-Met were used and the V'_{max} and K' at different fixed concentrations of substrate H3P20 were derived from the initial velocity studies. The concentrations of each substrates and corresponding V'_{max} and K' for each secondary plot are listed in Table S1. Then, the V'_{max} and K' were fitted using the Equations 3–6, 9–14 to obtain the kinetic parameters and the dependency of V'_{max} and K' on substrate H3P20 and AdoMet, respectively. The best-fit model was chosen based on the best coefficient of determination and lowest standard error of estimate. To ensure the accuracy of the analyses, the coefficient of determination, standard error of estimate, and sum of squares are presented in Table S5.

Inhibition studies

For the dead-end analogue inhibition experiments, either an H3 peptide with acetylation on K4 (H3P20Ac) or sinefungin was used as the dead-end analogue. Product inhibition assays were performed using either AdoHcy or the methylated H3 peptide (H3P20me). The inhibition experiments *versus* AdoMet were conducted with unsaturating H3 peptide concentration due to the limited availability of H3. For the inhibition assays, inhibitors were preincubated in buffer with M3RA or M4RA for 15 min. All dead-end inhibition studies and product inhibition study with H3P20me were performed using the methodology described previously, with the exception of adding different inhibitors. Assays with the dead-end inhibitor H3P20Ac at concentrations of 0, 200, and 400 μM were performed with constant (200 μM) or variable (0, 3.125, 6.25, 12.5, 25, 50, 100, 200 μM) AdoMet and constant (400 μM) or variable (0, 25, 50, 100, 200, 400, 800 μM) H3P20. Assays with the dead-end inhibitor sinefungin at concentrations of 0, 50, and 100 μM were performed with constant (200 μM) or variable (0, 3.125, 6.25, 12.5, 25, 50, 100, 200 μM) AdoMet and constant (400 μM) or variable (0, 25, 50, 100, 200, 400, 800 μM) H3P20. Assays with the product inhibitor H3P20me1 at concentrations of 0, 100, and 300 μM were performed with constant (200 μM) or variable (0, 3.125, 6.25, 12.5, 25, 50, 100, 200 μM) AdoMet and constant (400 μM) or variable (0, 25, 50, 100, 200, 400, 800 μM) H3P20. For product inhibition study with AdoHcy as the inhibitor, the mass-spectrometry-based methylation assays were performed. Constant (200 μM) or variable (0, 3.125, 6.25, 12.5, 25, 50, 100, 200 μM) AdoMet and constant (400 μM) or variable (0, 25, 50, 100, 200, 400, 800 μM) H3P20 were used in these assays. AdoMet and the
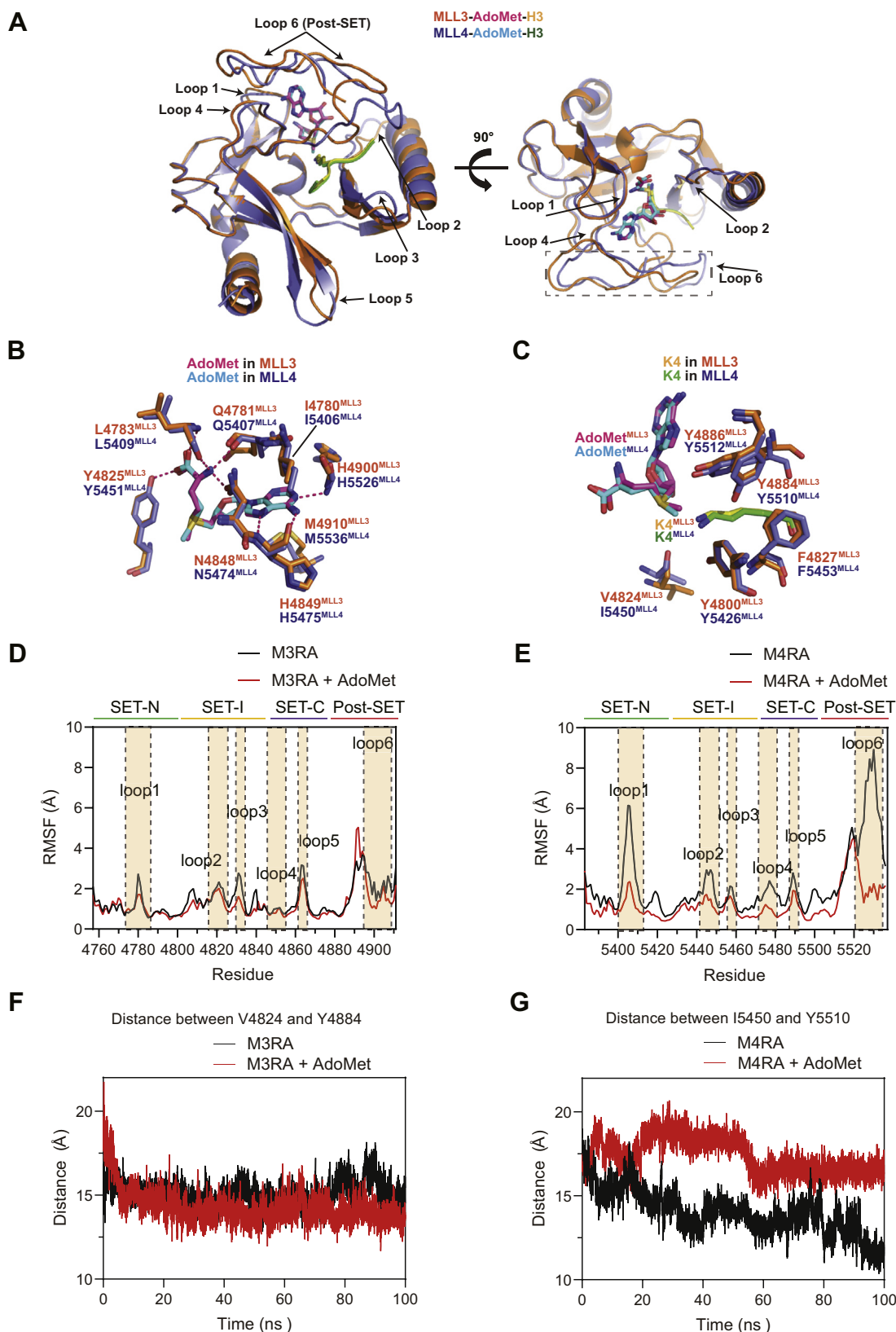
Figure 8. Molecular dynamics (MD) simulation of M3RA and M4RA. *A*, structural comparison of MLL3$_{SET}$ and MLL4$_{SET}$ suggests that the SET domain showed almost identical conformations in the MRA complex except the loop regions (Loop1–6). *B*, comparison of the AdoMet binding pocket of MLL3 and MLL4. Residues important for the AdoMet-MLL3$_{SET}$ and AdoMet-MLL4$_{SET}$ interaction are shown in *stick models*. Hydrogen bonds are indicated by *dashed lines*. *C*, comparison of the active center of MLL3 and MLL4. Residues important for the H3K4-MLL3$_{SET}$ and H3K4-MLL4$_{SET}$ interaction are shown in *stick models*. Root mean square fluctuation (RMSF) of the MLL3$_{SET}$ (*D*) and MLL4$_{SET}$ (*E*) with (*red line*) and without (*black line*) the association of AdoMet. Molecular dynamics simulation shows dynamics of the substrate H3-binding pocket of M3RA (*F*) and M4RA (*G*) with (*red line*) and without (*black line*) the binding of AdoMet.

H3P20 peptide were preincubated in 25 mM Tris buffer, pH 8.0 at 30 °C. The reaction was initiated by adding the pre-mixture of enzyme and 0, 50, 100 μM AdoHcy. In total, 5 μl reaction solution was taken out every 30 s and quenched by adding TFA to a final concentration of 0.5% and cooling at 4 °C. The product H3P20me1 was measured by MALDI-TOF MS as described above. Data were interpreted by both linear and nonlinear analyses. Lineweaver–Burk plots were generated according to the Equation 15. For nonlinear analyses, each data set was fit to equations corresponding to competitive (Equation 16), noncompetitive (Equation 17), and uncompetitive (Equation 18) inhibition. Data sets were assessed as best fitting to models based on the best coefficient of determination and the lowest error.

$$\frac{1}{v} = \frac{(1 + [I]/K_{ia})K_m}{V_{max}}\frac{1}{[S]} + \frac{1 + [I]/K_{ib}}{V_{max}} \qquad (15)$$

$$v = \frac{V_{max}[S]}{K_m(1 + [I]/K_I) + [S]} \qquad (16)$$

$$v = \frac{V_{max}[S]}{K_m + [S](1 + [I]/K_I)} \qquad (17)$$

$$v = \frac{V_{max}[S]}{K_m(1 + [I]/K_I + [S](1 + [I]/K_I)} \qquad (18)$$

Isothermal titration calorimetry

The equilibrium dissociation constants of AdoMet binding to M3RA and M4RA were determined by an ITC200 calorimeter (GE healthcare). The binding of proteins (50 μM) and cofactor AdoMet (1 mM) were measure in the 25 mM Tris-HCl, pH 8.0, 150 mM NaCl at 20 °C. ITC data were analyzed and fit using Origin 7 (OriginLab) using one-site model.

Fluorescence polarization assay

Equilibrium dissociation constants for the interaction of MAR proteins with FAM labeled H3 peptides were determined using fluorescence polarization (FP) assays. MAR proteins were diluted with assay buffer (20 mM HEPES, 150 mM NaCl, 0.1% BSA, pH7.4) to a serial of concentrations from 300 μM to 10 nM in a volume of 15 μl. The FAM labeled H3 peptides were mixed with MAR proteins at a final concentration of 100 nM in a final volume of 30 μl. The reaction mixtures were incubated at 25 °C in dark for 30 min, and the fluorescence polarization values were measured using Synergy Neo Multi-Mode Microplate Reader (Bio-Tek). Fluorescence was quantitated with GEN5, and the Kd values were calculated by fitting the sigmoidal dose–response equation with Prism8 software (GraphPad).

Molecular dynamics simulations parameters and setup

The M3RA structure was retrieved from RCSB PDB (PDB entry 5F6K). Since the M4RA structure is not available, the MLL4$_{SET}$ structure (PDB entry 4Z4P) was docked to the AR complex of the M3RA complex according to the M3RA structure. The N-terminals of MLL3$_{SET}$ and MLL4$_{SET}$ were adjusted to MLL3$_{SET}$ (4757S) and MLL4$_{SET}$ (5383S) respectively according to the alignment of Li *et al.* (14). The mutation in the crystal structure of MLL4$_{SET}$ was reversed by the mutagenesis plugin in PyMOL 2.3.4. All missing loops were repaired in UCSF Chimera 1.13.1 using the Modeller 9.24 (47, 48) with the DOPE protocol. All the hydrogen atoms of AdoMet were rebuilt using Builder in PyMOL 2.3.4 and double-checked in Avogadro 1.2.0n (49). The protonation states of Asp, Glu, His, Lys, Arg, and terminal residues were checked according to the prediction of PROPKA 3.0 (50)in the PDB2PQR server at pH 8.0, which is consistent to the experiments.

All simulations were performed using Gromacs 2018.4 (51) with CHARMM36 force field (52) and TIP3P water model (53). The prepared protein structures were centered in a cubic box with the minimum distance of 10 Å to the boundaries. Following solvation and charge neutralization to a final concentration of 0.1 M NaCl, the system went through unrestrained energy minimization *via* the steepest descent algorithm. The system was then gradually heated up to 300 K under NVT condition. NPT ensemble was then used to equilibrate the solvent and ions around the protein with the position of protein backbone, the zinc ion, and the AdoMet constrained with a harmonic potential of 1000 kJ/mol. The leap-frog integrator was used with the time step of 2 fs. V-rescale thermostat (54) was used to control the temperature at 300 K with the time constant of 0.1 ps. The Berendsen barostat (55) was used to control the pressure at 1 bar with the coupling constant of 2 ps. The Particle Mesh Ewald (PME) (56) method was used to determine the electrostatic interaction with the cutoff distance of 1.2 nm. van der Waals interactions were treated by using a switching function between 1.0 nm and 1.2 nm. After equilibration, we switched the temperature coupling to Parrinello–Rahman (57) and pressure coupling to Nose–Hoover (58) with coupling constants of 5 ps and 1 ps, respectively. The production phase of molecular dynamics simulation was conducted for 100 ns.

Molecular dynamics simulations analysis

The finished trajectory was first corrected for periodic boundary condition. A specific index file was created to designate the MLL$_{SET}$ of the M3RA or M4RA complex to ease further analysis. Further RMSF, distances, and free energy landscape were calculated only for MLL$_{SET}$ using built-in modules in Gromacs 2018.4. To be noted, RMSF calculations were conducted on the whole 100 ns timescale of the production phase of molecular dynamics simulation.

Data availability

All data generated or analyzed during this study are included in this published article and its supporting information, tables, or from the corresponding author upon request.

Conflicts of interest—The authors declare that they have no conflicts of interest with the contents of this article.

Abbreviations—The abbreviations used are: ABM, ASH2L-binding motif; AS, activation segment; IPTG, isopropyl 1-thio-β-D-galactopyranoside; k_{cat}, turnover number; k_{cat}/K_m, catalytic efficiency; M3RA, MLL3$_{SET}$-RBBP5$_{AS-ABM}$-ASH2L$_{SPRY}$; M4RA, MLL4$_{SET}$-RBBP5$_{AS-ABM}$-ASH2L$_{SPRY}$; M4WARD, MLL4-WDR5-ASH2L-RBBP5-DPY30; MLL, mixed-lineage leukemia; SET, SU(VAR)3–9, E(Z) and TRX; SPRY, splA and ryanodine receptor; ULP1, ubiquitin-like-specific protease 1.

References

1. Benjamin, D. Y., Hess, J. L., Horning, S. E., Brown, G. A., and Korsmeyer, S. J. (1995) Altered Hox expression and segmental identity in MLL-mutant mice. *Nature* **378**, 505–508
2. Jude, C. D., Climer, L., Xu, D., Artinger, E., Fisher, J. K., and Ernst, P. (2007) Unique and independent roles for MLL in adult hematopoietic stem cells and progenitors. *Cell Stem Cell* **1**, 324–337
3. Ang, S.-Y., Uebersohn, A., Spencer, C. I., Huang, Y., Lee, J.-E., Ge, K., and Bruneau, B. G. (2016) KMT2D regulates specific programs in heart development via histone H3 lysine 4 di-methylation. *Development* **143**, 810–821
4. Lee, J. E., Wang, C., Xu, S., Cho, Y. W., Wang, L., Feng, X., Baldridge, A., Sartorelli, V., Zhuang, L., Peng, W., and Ge, K. (2013) H3K4 mono- and di-methyltransferase MLL4 is required for enhancer activation during cell differentiation. *Elife* **2**, e01503
5. Collins, B. E., Greer, C. B., Coleman, B. C., and Sweatt, J. D. (2019) Histone H3 lysine K4 methylation and its role in learning and memory. *Epigenetics Chromatin* **12**, 1–16
6. Rao, R. C., and Dou, Y. (2015) Hijacked in cancer: The KMT2 (MLL) family of methyltransferases. *Nat. Rev. Cancer* **15**, 334–346
7. Krivtsov, A. V., and Armstrong, S. A. (2007) MLL translocations, histone modifications and leukaemia stem-cell development. *Nat. Rev. Cancer* **7**, 823–833
8. Meeks, J. J., and Shilatifard, A. (2017) Multiple roles for the MLL/COMPASS family in the epigenetic regulation of gene expression and in cancer. *Annu. Rev. Cancer Biol.* **1**, 425–446
9. Wang, P., Lin, C., Smith, E. R., Guo, H., Sanderson, B. W., Wu, M., Gogol, M., Alexander, T., Seidel, C., and Wiedemann, L. M. (2009) Global analysis of H3K4 methylation defines MLL family member targets and points to a role for MLL1-mediated H3K4 methylation in the regulation of transcriptional initiation by RNA polymerase II. *Mol. Cell. Biol.* **29**, 6074–6085
10. Hu, D., Garruss, A. S., Gao, X., Morgan, M. A., Cook, M., Smith, E. R., and Shilatifard, A. (2013) The Mll2 branch of the COMPASS family regulates bivalent promoters in mouse embryonic stem cells. *Nat. Struct. Mol. Biol.* **20**, 1093
11. Hu, D., Gao, X., Morgan, M. A., Herz, H.-M., Smith, E. R., and Shilatifard, A. (2013) The MLL3/MLL4 branches of the COMPASS family function as major histone H3K4 monomethylases at enhancers. *Mol. Cell. Biol.* **33**, 4745–4754
12. Herz, H. M., Mohan, M., Garruss, A. S., Liang, K., Takahashi, Y.-h., Mickey, K., Voets, O., Verrijzer, C. P., and Shilatifard, A. (2012) Enhancer-associated H3K4 monomethylation by Trithorax-related, the Drosophila homolog of mammalian Mll3/Mll4. *Genes Dev.* **26**, 2604–2620
13. Dou, Y., Milne, T. A., Ruthenburg, A. J., Lee, S., Lee, J. W., Verdine, G. L., Allis, C. D., and Roeder, R. G. (2006) Regulation of MLL1 H3K4 methyltransferase activity by its core components. *Nat. Struct. Mol. Biol.* **13**, 713–719
14. Li, Y., Han, J., Zhang, Y., Cao, F., Liu, Z., Li, S., Wu, J., Hu, C., Wang, Y., Shuai, J., Chen, J., Cao, L., Li, D., Shi, P., Tian, C., *et al.* (2016) Structural basis for activity regulation of MLL family methyltransferases. *Nature* **530**, 447–452
15. Cho, Y. W., Hong, T., Hong, S., Guo, H., Yu, H., Kim, D., Guszczynski, T., Dressler, G. R., Copeland, T. D., Kalkum, M., and Ge, K. (2007) PTIP associates with MLL3- and MLL4-containing histone H3 lysine 4 methyltransferase complex. *J. Biol. Chem.* **282**, 20395–20406
16. Dhar, S. S., Lee, S. H., Kan, P. Y., Voigt, P., Ma, L., Shi, X., Reinberg, D., and Lee, M. G. (2012) Trans-tail regulation of MLL4-catalyzed H3K4 methylation by H4R3 symmetric dimethylation is mediated by a tandem PHD of MLL4. *Genes Dev.* **26**, 2749–2762
17. Liu, Y., Qin, S., Chen, T. Y., Lei, M., Dhar, S. S., Ho, J. C., Dong, A., Loppnau, P., Li, Y., Lee, M. G., and Min, J. (2019) Structural insights into trans-histone regulation of H3K4 methylation by unique histone H4 binding of MLL3/4. *Nat. Commun.* **10**, 36
18. Zhang, Y., Jang, Y., Lee, J. E., Ahn, J., Xu, L., Holden, M. R., Cornett, E. M., Krajewski, K., Klein, B. J., Wang, S. P., Dou, Y., Roeder, R. G., Strahl, B. D., Rothbart, S. B., Shi, X., *et al.* (2019) Selective binding of the PHD6 finger of MLL4 to histone H4K16ac links MLL4 and MOF. *Nat. Commun.* **10**, 2314
19. Ashokkumar, D., Zhang, Q., Much, C., Bledau, A. S., Naumann, R., Alexopoulou, D., Dahl, A., Goveas, N., Fu, J., and Anastassiadis, K. (2020) MLL4 is required after implantation, whereas MLL3 becomes essential during late gestation. *Development* **147**, dev186999
20. Wang, C., Lee, J.-E., Lai, B., Macfarlan, T. S., Xu, S., Zhuang, L., Liu, C., Peng, W., and Ge, K. (2016) Enhancer priming by H3K4 methyltransferase MLL4 controls cell fate transition. *Proc. Natl. Acad. Sci. U. S. A.* **113**, 11871–11876
21. Faundes, V., Malone, G., Newman, W. G., and Banka, S. (2019) A comparative analysis of KMT2D missense variants in Kabuki syndrome, cancers and the general population. *J. Hum. Genet.* **64**, 161–170
22. Yan, J., Chen, S. A., Local, A., Liu, T., Qiu, Y., Dorighi, K. M., Preissl, S., Rivera, C. M., Wang, C., Ye, Z., Ge, K., Hu, M., Wysocka, J., and Ren, B. (2018) Histone H3 lysine 4 monomethylation modulates long-range chromatin interactions at enhancers. *Cell Res.* **28**, 204–220
23. Jang, Y., Wang, C., Zhuang, L., Liu, C., and Ge, K. (2017) H3K4 methyltransferase activity is required for MLL4 protein stability. *J. Mol. Biol.* **429**, 2046–2054
24. Jang, Y., Broun, A., Wang, C., Park, Y. K., Zhuang, L., Lee, J. E., Froimchuk, E., Liu, C., and Ge, K. (2018) H3. 3K4M destabilizes enhancer H3K4

ASBMB

methyltransferases MLL3/MLL4 and impairs adipose tissue development. *Nucleic Acids Res.* **47**, 607–620

25. Zhang, Y., Mittal, A., Reid, J., Reich, S., Gamblin, S. J., and Wilson, J. R. (2015) Evolving catalytic properties of the MLL family SET domain. *Structure* **23**, 1921–1933

26. Bolhuis, P. A., Zwart, R., Bär, P. R., De Visser, M., and van der Helm, H. J. (2019) Rapid determination of the hypoxanthine increase in ischemic exercise tests. *Clin. Chem.* **34**, 1607–1610

27. Dorgan, K. M., Wooderchak, W. L., Wynn, D. R. P., Karschner, E. L., Alfaro, J. F., Cui, Y., Zhou, Z. S., and Hevel, J. M. (2006) An enzyme-coupled continuous spectrophotometric assay for S-adenosylmethionine-dependent methyltransferases. *Anal. Biochem.* **350**, 249–255

28. Marangoni, A. G. (2003) *Enzyme Kinetics: A Modern Approach*, John Wiley & Sons, New York, NY

29. Cleland, W. W. (1963) The kinetics of enzyme-catalyzed reactions with two or more substrates or products: I. Nomenclature and rate equations. *Biochim. Biophys. Acta* **67**, 104–113

30. Purich, D. L. (2009) *Contemporary Enzyme Kinetics and Mechanism*, Reliable Lab Solutions, Academic Press, Oxford, UK

31. Leskovac, V. (2003) *Comprehensive Enzyme Kinetics*, Springer Science & Business Media, New York, NY

32. Weinberg, D. N., Allis, C. D., and Lu, C. (2017) Oncogenic mechanisms of histone H3 mutations. *Cold Spring Harb. Perspect. Med.* **7**, a026443

33. Ibáñez, G., McBean, J. L., Astudillo, Y. M., and Luo, M. (2010) An enzyme-coupled ultrasensitive luminescence assay for protein methyltransferases. *Anal. Biochem.* **401**, 203–210

34. Schapira, M. (2011) Structural chemistry of human SET domain protein methyltransferases. *Curr. Chem. Genomics* **5**, 85–94

35. Patnaik, D., Chin, H. G., Esteve, P. O., Benner, J., Jacobsen, S. E., and Pradnan, S. (2004) Substrate specificity and kinetic mechanism of mammalian G9a histone H3 methyltransferase. *J. Biol. Chem.* **279**, 53248–53258

36. Chin, H. G., Patnaik, D., Esteve, P. O., Jacobsen, S. E., and Pradhan, S. (2006) Catalytic properties and kinetic mechanism of human recombinant Lys-9 histone H3 methyltransferase SUV39H1: Participation of the chromodomain in enzymatic catalysis. *Biochemistry* **45**, 3272–3284

37. Zheng, W., Ibáñez, G., Wu, H., Blum, G., Zeng, H., Dong, A., Li, F., Hajian, T., Allali-Hassani, A., and Amaya, M. F. (2012) Sinefungin derivatives as inhibitors and structure probes of protein lysine methyltransferase SETD2. *J. Am. Chem. Soc.* **134**, 18004–18014

38. Shiraki, N., Shiraki, Y., Tsuyama, T., Obata, F., Miura, M., Nagae, G., Aburatani, H., Kume, K., Endo, F., and Kume, S. (2014) Methionine metabolism regulates maintenance and differentiation of human pluripotent stem cells. *Cell Metab.* **19**, 780–794

39. Hermes, M., von Hippel, S., Osswald, H., and Kloor, D. (2005) S-adenosylhomocysteine metabolism in different cell lines: Effect of hypoxia and cell density. *Cell Physiol. Biochem.* **15**, 233–244

40. Longnecker, D. S. (2002) Abnormal methyl metabolism in pancreatic toxicity and diabetes. *J. Nutr.* **132**, 2373S–2376S

41. MacLennan, N. K., James, S. J., Melnyk, S., Piroozi, A., Jernigan, S., Hsu, J. L., Janke, S. M., Pham, T. D., and Lane, R. H. (2004) Uteroplacental insufficiency alters DNA methylation, one-carbon metabolism, and histone acetylation in IUGR rats. *Physiol. Genomics* **18**, 43–50

42. Kandoth, C., McLellan, M. D., Vandin, F., Ye, K., Niu, B., Lu, C., Xie, M., Zhang, Q., McMichael, J. F., Wyczalkowski, M. A., Leiserson, M. D. M., Miller, C. A., Welch, J. S., Walter, M. J., Wendl, M. C., *et al.* (2013) Mutational landscape and significance across 12 major cancer types. *Nature* **502**, 333–339

43. Daigle, S. R., Olhava, E. J., Therkelsen, C. A., Basavapathruni, A., Jin, L., Boriack-Sjodin, P., Allain, C. J., Klaus, C. R., Raimondi, A., and Scott, M. P. (2013) Potent inhibition of DOT1L as treatment of MLL-fusion leukemia. *Blood* **122**, 1017–1025

44. Barsyte-Lovejoy, D., Li, F., Oudhoff, M. J., Tatlock, J. H., Dong, A., Zeng, H., Wu, H., Freeman, S. A., Schapira, M., and Senisterra, G. A. (2014) (R)-PFI-2 is a potent and selective inhibitor of SETD7 methyltransferase activity in cells. *Proc. Natl. Acad. Sci. U. S. A.* **111**, 12853–12858

45. Schapira, M. (2016) Chemical inhibition of protein methyltransferases. *Cell Chem. Biol.* **23**, 1067–1076

46. Stein, R. L. (2011) *Kinetics of Enzyme Action: Essential Principles for Drug Hunters*, John Wiley & Sons, New York, NY

47. Eswar, N., Webb, B., Marti-Renom, M. A., Madhusudhan, M., Eramian, D., Shen, M. Y., Pieper, U., and Sali, A. (2006) Comparative protein structure modeling using Modeller. *Curr. Protoc. Bioinformatics* **15**, 5–6

48. Fiser, A., Do, R. K. G., and Šali, A. (2000) Modeling of loops in protein structures. *Protein Sci.* **9**, 1753–1773

49. Hanwell, M. D., Curtis, D. E., Lonie, D. C., Vandermeersch, T., Zurek, E., and Hutchison, G. R. (2012) Avogadro: An advanced semantic chemical editor, visualization, and analysis platform. *J. Cheminformatics* **4**, 1–17

50. Søndergaard, C. R., Olsson, M. H., Rostkowski, M., and Jensen, J. H. (2011) Improved treatment of ligands and coupling effects in empirical calculation and rationalization of pKa values. *J. Chem. Theor. Comput.* **7**, 2284–2295

51. Berendsen, H. J., van der Spoel, D., and van Drunen, R. (1995) Gromacs: A message-passing parallel molecular dynamics implementation. *Comput. Phys. Commun.* **91**, 43–56

52. Huang, J., and MacKerell, A. D., Jr. (2013) CHARMM36 all-atom additive protein force field: Validation based on comparison to NMR data. *J. Comput. Chem.* **34**, 2135–2145

53. Jorgensen, W. L., Chandrasekhar, J., Madura, J. D., Impey, R. W., and Klein, M. L. (1983) Comparison of simple potential functions for simulating liquid water. *J. Chem. Phys.* **79**, 926–935

54. Bussi, G., Donadio, D., and Parrinello, M. (2007) Canonical sampling through velocity rescaling. *J. Chem. Phys.* **126**, 014101

55. Berendsen, H. J., Postma, J. V., van Gunsteren, W. F., DiNola, A., and Haak, J. R. (1984) Molecular dynamics with coupling to an external bath. *J. Chem. Phys.* **81**, 3684–3690

56. Essmann, U., Perera, L., Berkowitz, M. L., Darden, T., Lee, H., and Pedersen, L. G. (1995) A smooth particle mesh Ewald method. *J. Chem. Phys.* **103**, 8577–8593

57. Parrinello, M., and Rahman, A. (1981) Polymorphic transitions in single crystals: A new molecular dynamics method. *J. Appl. Phys.* **52**, 7182–7190

58. Evans, D. J., and Holian, B. L. (1985) The Nose–Hoover thermostat. *J. Chem. Phys.* **83**, 4069–4074

59. Madeira, F., Park, Y. M., Lee, J., Buso, N., Gur, T., Madhusoodanan, N., Basutkar, P., Tivey, A. R. N., Potter, S. C., Finn, R. D., and Lopez, R. (2019) The EMBL-EBI search and sequence analysis tools APIs in 2019. *Nucleic Acids Res.* **47**, W636–W641